International Journal of Nanomedicine

Dovepress
Taylor & Francis Group

Open Access Full Text Article

ORIGINAL RESEARCH

Dynamic Covalent Bond-Based Nanoassembly of Curcumin to Enhance the Selective Photothermal Therapy for Tumor Treatment

Jiamin Qin[1,*], Guojuan Fan[2,*], Yanna Lv[1,*], Junxiao Zhang[1], Shenglin Geng[1], Lan Ma[1], Ling Wang[1], Jiaxin Yang[3,4], Weifen Zhang[1,5,6], Yizhou Zhan[3,4], Xiaoji Wang[4,7], Jinlong Ma[1,5,6]

[1]School of Pharmacy, Shandong Second Medical University, Weifang, Shandong, 261053, People's Republic of China; [2]Dermatology, Weifang Hospital of Traditional Chinese Medicine, Shandong Second Medical University, Weifang, Shandong, 261000, People's Republic of China; [3]School of Materials Science and Engineering, Dongguan University of Technology, Dongguan, Guangdong Province, 523808, People's Republic of China; [4]Songshan Lake Innovation Center of Medicine and Engineering, Dongguan University of Technology, Dongguan, Guangdong Province, 523808, People's Republic of China; [5]Collaborative Innovation Center for Target Drug Delivery System, Shandong Second Medical University, Weifang, Shandong, 261053, People's Republic of China; [6]Shandong Engineering Research Center for Smart Materials and Regenerative Medicine, Shandong Second Medical University, Weifang, Shandong, 261053, People's Republic of China; [7]School of Chemical Engineering and Energy Technology, Dongguan University of Technology, Dongguan, Guangdong Province, 523808, People's Republic of China

*These authors contributed equally to this work

Correspondence: Yizhou Zhan; Jinlong Ma, Email zhanyizhou@dgut.edu.cn; majinlong99@hotmail.com

Introduction: Owing to the uneven distribution of photothermal agents (PTAs), photothermal therapy (PTT) can damage normal tissues. The dynamic reversible covalent bond, which can significantly improve the oxidation stability of the drug and the characteristics of responsive drug release, thus improving the conversion efficiency of the drug, is a feasible solution to enhance the selective PTT for tumor treatment.

Methods: The nanoassembly loaded curcumin (Cur) with dynamic covalent boronate and encapsulated Indocyanine Green (ICG) in the phospholipid bilayer by dynamic self-assembly.

Results: The pH-responsive dynamic covalent bond-based nanoassembly system has great selective release of drugs in the tumor microenvironment and photothermal conversion efficiency. Furthermore, LIP-C/I could increase the antitumor effect through the combination of PTT and chemotherapy (CT). The experiments in vitro and in vivo have demonstrated that LIP-C/I could enhance selective PTT for tumor treatment.

Discussion: Our nanoassembly system provides an alternative approach for enhancing selective PTT for tumor treatment using dynamic covalent boronate.

Keywords: dynamic covalent bond, nanoassembly, curcumin, photothermal therapy, tumor treatment

Introduction

Cancer has emerged as one of the most pressing global health challenges, with 2022 statistics revealing a staggering 20 million new diagnoses and nearly 10 million deaths worldwide.[1,2] Despite extensive efforts, the incidence of cancer continues to rise, underscoring the urgent need for innovative therapeutic strategies.[3] Photothermal therapy (PTT), which converts light energy into heat to ablate tumors using photothermal agents (PTAs), has gained attention for its minimal invasiveness, high efficiency, and spatiotemporal precision.[4–7] However, the uneven distribution of PTAs often leads to collateral damage to healthy tissues, limiting its clinical potential.[8–11]

Owing to their lower toxicity, controlled release of the drug, and improved bioavailability,[12] liposomes have the potential to address these limitations by improving PTT selectivity. Boronate ester bonds are pH-sensitive groups formed by boronic acids and 1.2- or 1.3-diol in an alkaline solution, and the borate complex can dissociate at acidic pH.[13–16] Unlike conventional liposomes, which rely on weak interactions for drug encapsulation, the liposomes that leverage dynamic covalent boronate chemistry could significantly improve encapsulation efficiency and drug loading capacity.[17] Importantly, dynamic reversible

Received: 27 December 2024
Accepted: 20 March 2025
Published: 30 March 2025

Graphical Abstract

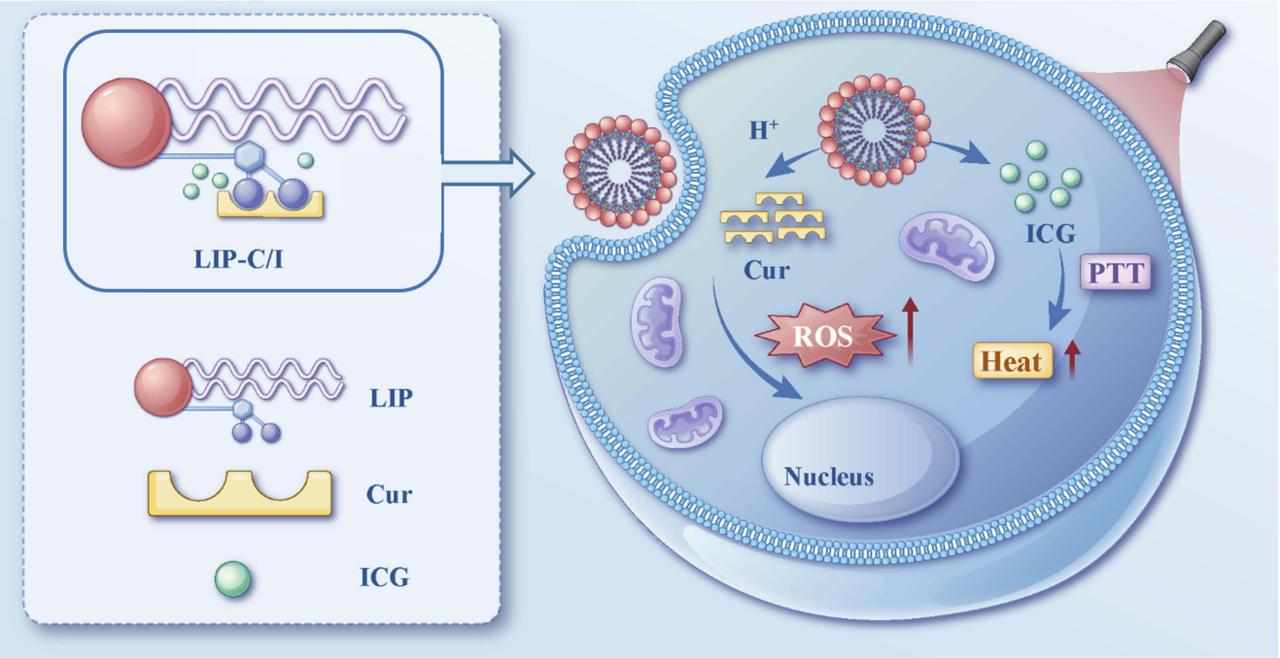

covalent bonds could improve the oxidation stability of the drug and the characteristics of responsive drug release, thus improving the conversion efficiency of the drug in the nanoparticles (NPs) transport system.[18,19] By integrating dynamic covalent strategies, the liposomes offer a simple and robust platform for achieving precise and selective tumor treatment, marking a significant advancement in PTT.[20,21]

Natural medicines have good biological activity and pharmacological effects and can achieve antitumor activity and selectivity by the application of scientific methods to provide a choice for the treatment of cancer.[22–25] Curcumin (Cur), a well-studied natural compound with anti-inflammatory, antioxidant, and anticancer properties, is employed as a complementary agent to enhance the selectivity of PTT.[18,26–28] Although the antitumor efficacy of Cur is limited by its poor solubility and bioavailability, dynamic covalent bond-based NPs could effectively address these challenges.[29,30] By encapsulating Cur within dynamic covalent bonds, researchers could improve its solubility, bioavailability, and tumor-specific release, thereby maximizing its therapeutic potential.

Herein, we designed a pH-responsive nanoassembly system (Scheme 1) loaded with Cur using a dynamic covalent boronate and encapsulated Indocyanine Green (ICG) in the phospholipid layer to increase the solubility of Cur and reduce the degradation of ICG. ICG and Cur can be released in response to the tumor acidic environment to increase their antitumor effect through the combination of PTT and chemotherapy (CT). This work provides not only an alternative approach to enhance selective PTT for tumor treatment using dynamic covalent boronate, but also a nano-drug delivery platform for natural medicines.

Experimental

Materials

ICG, Cur, and calcein-AM/PI Double Stain Kit were acquired from American Apexbio Biotech. Ltd. Co. 3-(4,5-dimethyl-2-thiazolyl)-2,5-diphenyl-2-*H*-tetrazolium bromide (MTT) was purchased from Shanghai Beyotime Biotechnology Co., Ltd. The Annexin V FITC Apoptosis Detection Kit was sourced from BD. (USA). 4T1 Cell lines, 231 Cell lines, and L929 cell lines were obtained from American Type Culture Collection (ATCC). No additional purification was performed on any of the chemicals prior to their use.

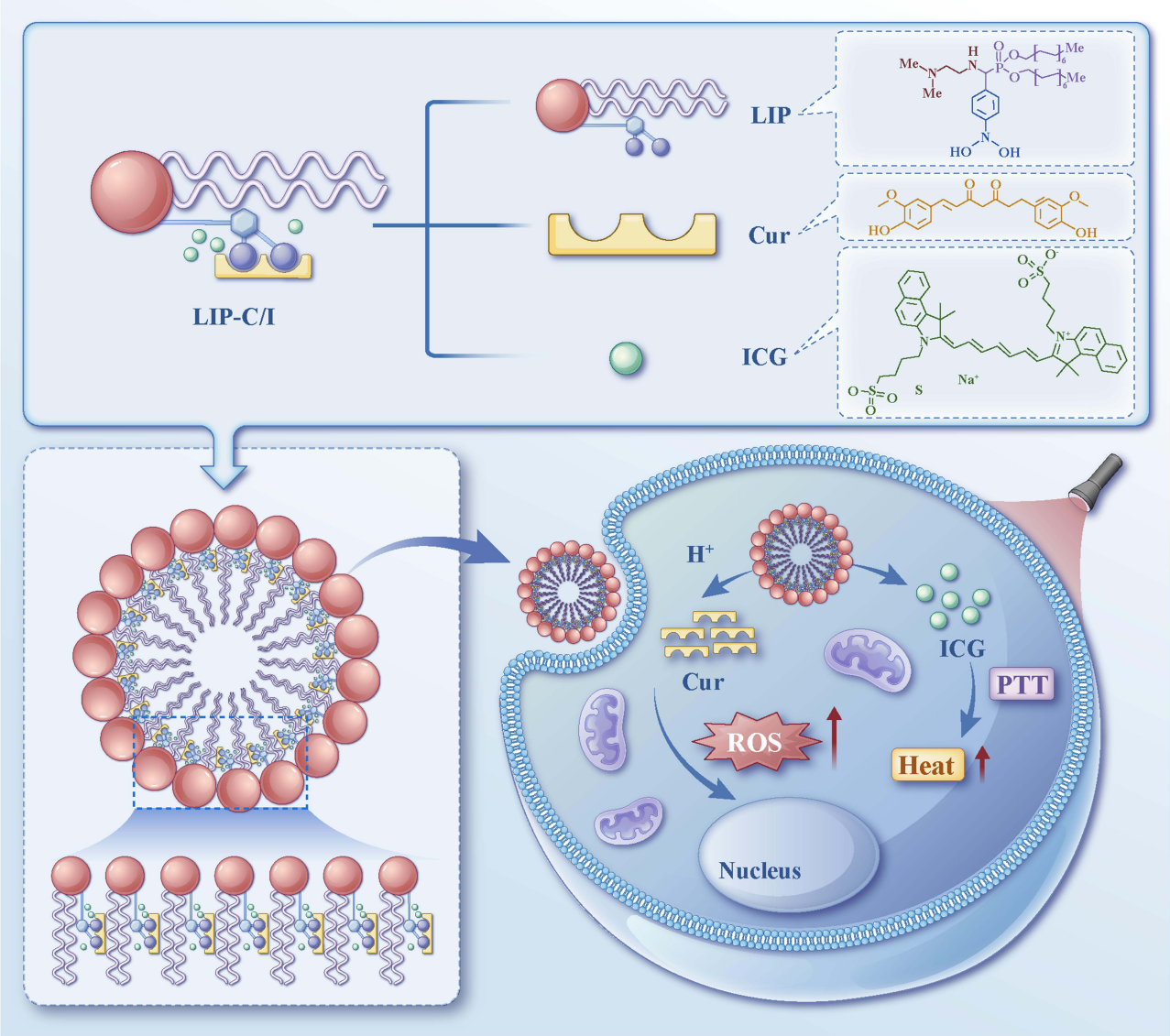

Scheme 1 Schematic illustration of the formation and mechanism of the LIP-C/I.

Preparation of NPs

Preparation of LIP

N, N-dimethylethylenediamine (55.1 μL, 0.5 mmol) was added to a methanol (1 mL) solution of 4-formylphenylboronic acid (74.9 mg, 0.5 mmol), heated to 70°C, and reacted for 3 h, under nitrogen protection. After the reaction was complete, the temperature was reduced to room temperature, the solvent was evaporated by rotation, and the crude product of the imine intermediate was directly used for the next step of the reaction.

Preparation of LIP-C/I

ICG (1 mg/mL, 1165 μL), Cur (1 mg/mL, 370 μL), and LIP (10 mg/mL, 72.5 μL) were mixed and stirred for 3 min under magnetic agitation to prepare the LIP-C/I solution.

Characterization

The particle size and zeta potential of the LIP-C/I solution were measured using a Zetasizer Nano ZS90 instrument. An ultraviolet spectrophotometer (Evolution 300, Thermo, US) was utilized to scan the nanoparticles across the wavelength

https://doi.org/10.2147/IJN.S512590

range of 200–800 nm. Additionally, a Fourier Transform Infrared Spectrometer (Avatar-360, PerkinElmer, Waltham, MA, USA) was employed to conduct infrared spectrum analysis of the nanoparticles within the wavenumber range of 400–4000 cm^{-1}. The morphology of the LIP-C/I was observed using transmission electron microscopy (TEM) to observe their morphology.

Drug Loading and Entrapment Efficiency

LIP-C/I (ICG: 385, 775, 1165, 1550, and 1935 μL) was centrifuged at 6500 rpm for 15 min. The supernatant was collected for absorbance measurements at 425 nm and 784 nm to determine free Cur and ICG concentrations, allowing for the calculation of the encapsulation efficiency (EE) of LIP-C/I. After centrifugation, the precipitate was rinsed with PBS thrice, and LIP-C/I samples were freeze-dried using a lyophilizer. The drug loading (DL) capacity of LIP-C/I was then determined after drying and weighing the samples. The DL and EE were ascertained through the subsequent equations:

$$\mathrm{DL}\ (\%) = (\mathrm{W_A} - \mathrm{W_B})/\mathrm{W_C} \times\ 100\%$$

$$\mathrm{EE}\ (\%) = (\mathrm{W_A} - \mathrm{W_B})/\mathrm{W_A} \times 100\%$$

Where W_A, W_B, and W_C denote the initial weights of Cur and ICG, the amount of free drug present in the supernatant, and the average freeze-dried weight of LIP-C/I, respectively.

In vitro Drug Release

The in vitro drug release characteristics of the LIP-C/I was assessed utilizing the dialysis-bag technique. The samples were encapsulated within a pre-conditioned dialysis bag with a molecular weight cutoff of 3500 Da. The dialysis bags were placed in a conical flask containing a release medium (PBS: pH 5.5, 6.5, 7.4) with or without 3.4 mmol/L hydrogen peroxide (H_2O_2) and placed in a constant-temperature oscillator at (37 ± 0.5)°C and 100 rpm. Samples of 1 mL dialysate were collected from the conical flask at time points of 0.5, 1, 2, 4, 6, 8, 12, 24, 36, and 48 hours, followed by the addition of an equal volume of fresh release medium. UV-Vis spectrophotometry was employed to measure the absorbance of LIP-C/I at wavelengths of 425 nm and 784 nm, thereby ascertaining the cumulative release amounts of Cur and ICG at pH levels of 5.5, 6.5, and 7.4. Subsequently, the cumulative release rates were calculated based on these measurements.

Photothermal Conversion Efficiency

LIP-C/I and ICG solutions with various concentrations (5, 10, 15, 20, and 25 μg/mL) were prepared. The solution was then irradiated for 5 min with an 808 nm laser (1.5 W/cm^2). Temperature readings were obtained using a near-infrared thermal imaging camera (FLIR ETS320), with subsequent data analysis conducted through the FLIR Tools software. In addition, the temperature changes in LIP-C/I and ICG (with an ICG concentration of 50 μg/mL) were assessed under various power densities (1, 1.5, and 2 W/cm^2). LIP-C/I and ICG (ICG concentration: 50 μg/mL) were irradiated with near-infrared light for 5 min and cooled at 25°C. Temperature was monitored using a thermal imaging camera during this period. The procedure was repeated five times to obtain cyclic curves and photostability.

In vitro Experiments

Hemolysis Test

Freshly collected blood samples from BALB/c mice were subjected to centrifugation at 5000 rpm for 10 minutes, followed by three washes with PBS until the supernatant became clear, yielding the red blood cells. The stock dispersion was prepared by mixing erythrocytes with saline in a ratio of 3:11 following centrifugation. The stock dispersion (100 μL stock dispersion was added to 1 mL of buffer containing Cur, ICG, and LIP-C/I at concentrations of 5, 10, 15, 20, and 25 μg/mL. Following a 3-hour incubation at 37°C, the mixture was subjected to centrifugation at 6500 rpm for 15 minutes. The absorbance of the resulting supernatant was then quantified at 540 nm using UV-visible spectroscopy. The hemolysis rate was calculated using the following formula:

$$\text{Hemolysis percentage}(\%) = (\mathrm{A_S} - \mathrm{A_N})/(\mathrm{A_P} - \mathrm{A_N}) \times 100$$

A_N and A_P denote the absorbance values of saline and deionized water, respectively, while A_S encompasses the absorbance readings for Cur, ICG, and LIP-C/I.

Cytotoxicity Test

To evaluate the biocompatibility of Cur, ICG, and LIP-C/I, L929 cells were utilized in an MTT assay. The cells were initially cultured in 100 μL of DMEM within 96-well plates at a density of 8,000 cells per well for 24 hours. Subsequently, they were treated with Cur, ICG, or LIP-C/I at concentrations ranging from 5 to 25 μg/mL and incubated at 37°C with 5% CO_2 for an additional 24 hours. Subsequently, 10 μL of MTT solution was added to each well, and the cells were cultured for an additional 4 hours. Afterward, the cells were rinsed with PBS and lysed with 100 μL of DMSO. Following the incubation, the absorbance in each well was measured at 490 nm using an automated microplate reader (Multiskan Go, USA), which is designed for enzyme-linked immunosorbent assay analysis.

Moreover, the therapeutic effect in vitro therapeutic effects of Cur, ICG, and LIP-C/I on cancer cells were assessed. MDA-MB-231 and 4T1 cells were seeded in 96-well plates at a density of 7,000 cells per well with 100 μL of RPMI medium and incubated for 12 hours, after which they were treated with Cur, ICG, ICG + NIR, LIP-C/I, or LIP-C/I + NIR at concentrations ranging from 5 to 25 μg/mL under conditions of 808 nm wavelength, 1.5 W/cm² power density, and 2 minutes of exposure. Cell viability was evaluated using an MTT assay. The experiment with L929 and MDA-MB-231 cells was performed again after changing the culture medium without the drug after four hours.

The LIVE/DEAD assay was employed to evaluate the in vitro therapeutic efficacy of Cur, ICG, and LIP-C/I. L929 cells and MDA-MB-231 cells were maintained in 2.0 mL culture medium in a 35 mm^2 cell culture dish (30 k per well) overnight. The cells were then treated with Cur, ICG, ICG+NIR, LIP-C/I, or LIP-C/I+NIR at a concentration of 20 μg/mL. Following treatment, the cells were gently rinsed twice with PBS. Subsequently, they were incubated with 200 μL of the AM/PI staining cocktail for 20 minutes, and the results were assessed using a fluorescence microscope. The experiment with L929 and MDA-MB-231 cells was performed again after changing the culture medium without the drug after four hours.

Flow cytometry was performed as follows: MDA-MB-231 cells were cultured with Cur, ICG, ICG+NIR, LIP-C/I, and LIP-C/I+NIR in 35 mm^2 cell culture dish for 24 h at a concentration of 20 μg/mL. The cells underwent digestion, were collected, and washed three times with PBS prior to staining with an Annexin-V/PI kit. Subsequently, they were analyzed using a flow cytometer (BD Pharmingen, CA, USA).

Assessment of Cellular Reactive Oxygen Species (ROS) Levels

MDA-MB-231 cells (1×10^5) were maintained in 2.0 mL culture medium in a 35 mm^2 cell culture dish (30 k per well) overnight. Then the cells were incubated with PBS, Cur, ICG, ICG+NIR, LIP-C/I, and LIP-C/I+NIR at the concentration of 20 μg/mL (1.5 W/cm^2, 3 min) for 24 h. Replace the cell culture medium with diluted 2′,7′-Dichlorofluorescin diacetate (10 μmol/L, 1 mL) solution and then incubate the cells at 37°C for 20 minutes. The ROS levels were quantified employing an inverted fluorescence microscope.

In vivo Experiments

Establishment of Animal Tumor Model

The right hind limbs of Female BALB/c mice (4–6 weeks) were subcutaneously injected with 100 μL of a PBS suspension containing 4T1 cells at a concentration of 1×10^6 cells/mL. The tumor model was considered established when the tumor volume approximated 100 mm^3.

Female BALB/c mice, aged 4–6 weeks with a body weight range of 18–20 g, were randomly assigned to two groups, each consisting of three animals. Cur, ICG, LIP-C/I, and saline were administered intraperitoneally to the BALB/c mice. Daily body weight measurements were taken for a period of 10 days. On the tenth day, the major organs, including the heart, liver, spleen, lungs, and kidneys, were harvested. These organs were then stained with hematoxylin and eosin (H&E), sectioned, and examined under a microscope for histological analysis.

In vivo Biodistribution and Photothermal Effect

The biodistribution and photothermal effect of ICG and LIP-C/I in tumor-bearing mice were assessed by the near infrared mouse imaging system (PE IVIS Spectrum) and thermal imaging camera. Both ICG (100 μL) and LIP-C/I were administered intraperitoneally to the mice. Whole-body optical imaging was conducted at predetermined time intervals: 2, 6, 12, 24, and 48 hours post-injection. Following the 6-hour and 8-hour time points, the mice were sacrificed, and the optical imaging data of the primary organs and tumors were collected and analyzed.

In vivo Antitumor Therapy

Upon reaching a tumor volume of approximately 100 mm^3, the mice were randomly assigned to eight groups, each consisting of five animals. Subsequently, these groups received treatments with PBS, PBS+NIR, Cur, Cur+NIR, ICG, and ICG+NIR, as well as LIP-C/I and LIP-C/I+NIR (ICG: 750 μg, 1.5 W/cm^2, 3 min). The treatment regimen spanned 14 days, involving a total of five injections. Concurrently, the body weights of the mice were meticulously monitored and documented daily throughout the two-week treatment period. Following this, the tumor-bearing mice were euthanized, and the tumors were harvested for subsequent weighing, documentation through photography, and histological examination via H&E staining.

Statistical Analysis: Data are presented as mean values ± standard deviation (SD), reflecting the outcomes of multiple experimental repetitions. Comparative analysis of the results was conducted using the *t*-test to determine significant differences.

Results and Discussion

Synthesis and Characterization

We first synthesized LIP in two steps, as illustrated in Figure S1. Subsequent nuclear magnetic resonance (NMR) and mass spectrometry (MS) analyses confirmed the chemical structure of LIP and its relatively stable nature (Figures S2 and S3). We then studied the dynamic covalent boronate interactions between LIP and boronic acid-bearing drugs by mixing LIP, Cur, and ICG in PBS (Scheme 1). When the resulting LIP-C/I was dispersed in PBS, nanoassemblies were formed owing to the amphiphilic nature of LIP-C/I. The as-prepared LIP-C/I nanoassemblies had a diameter of approximately 170.4±1.803 nm (PDI: 0.164±0.022), and spherical nanostructures were observed by TEM (Figure 1a and b). The UV-Vis absorption spectra showed clear peaks at 425 and 784 nm (Figure 1c). The chemical structure of LIP-C/I was further characterized. After the reaction, the absorbance peak at 16 ppm disappeared and a new peak at approximately 6 ppm appeared in the corresponding NMR spectra (Figure 1d). In the subsequent Fourier transform infrared (FTIR) spectroscopy, the vibration peaks of B-OH were replaced by those of B-O-C (Figure 1e). These results collectively suggested the reaction of the diketone structure with boronic acid and the formation of a boronate ester. The size and zeta potential showed no notable change after one week, illustrating that LIP-C/I had great storage stability (Figure S4). The critical aggregation concentration (CAC) of LIP-C/I was measured to be 0.2239 μg/mL (Figure S5).

The drug delivery ability was investigated by loading different proportions of ICG into LIP-C/I, and the drug release characteristics are shown in Table S1. The DL capacity of LIP-C/I progressively enhanced as the concentrations were elevated. Following a comprehensive assessment of DL and EE, a molar ratio of 1.5:1 for ICG to Cur was determined to be optimal for nanoparticle preparation, which was then used in the subsequent experiments.

Drug Release in vitro

Selective release of drugs in the tumor microenvironment is an important factor in enhancing tumor selective killing. As shown in Figure 2a and b, the release rate of LIP-C/I was high, the cumulative release amount was high within 12 h, and the release slowed significantly. At the same time, the release rate of LIP-C/I was fastest at pH 5.0, followed by pH 6.5, and the lowest in the release medium at pH 7.4, which could help reduce toxicity to normal tissues. Following a 48-hour period, the release rate of ICG from LIP-C/I reached approximately 36.8% at pH 6.0 and 13.2% at pH 7.4, whereas at pH 5.0, nearly 54.0% of ICG was released. The release rate of the drug Cur in LIP-C/I was approximately 40.6% and 15.6% at pH 6.0 and pH 7.4, respectively, while 60.6% Cur release was observed at pH 5.0 (Figure 2c). Under H_2O_2 conditions, 56.9% of ICG was released at pH 5.0, and 67.2% was released at pH 5.0, with an increase in drug release compared to no H_2O_2 (Figure 2d and f). The release of Cur also has a higher release with H_2O_2 than without H_2O_2 (Figure 2e). Thus, nanoparticles can exert antitumor activity by responding to intracellular stimuli through triggered drug release in the tumor environment.

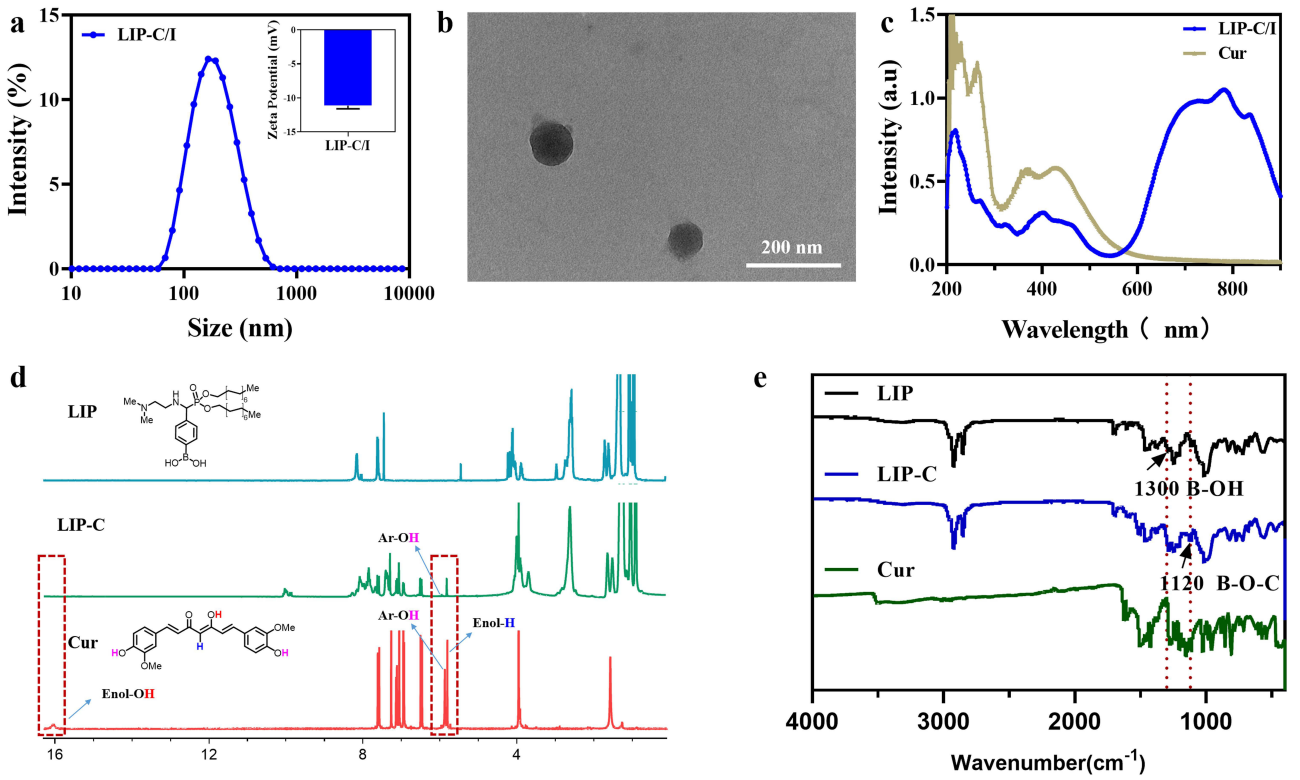

Figure 1 (**a**) DLS profile and Zeta potential, (**b**) TEM images, and (**c**) UV-vis absorbance spectra of LIP-C/I and free Cur. (**d**) ^{1}H NMR and (**e**) FTIR spectra of LIP, LIP+Cur, and Cur.

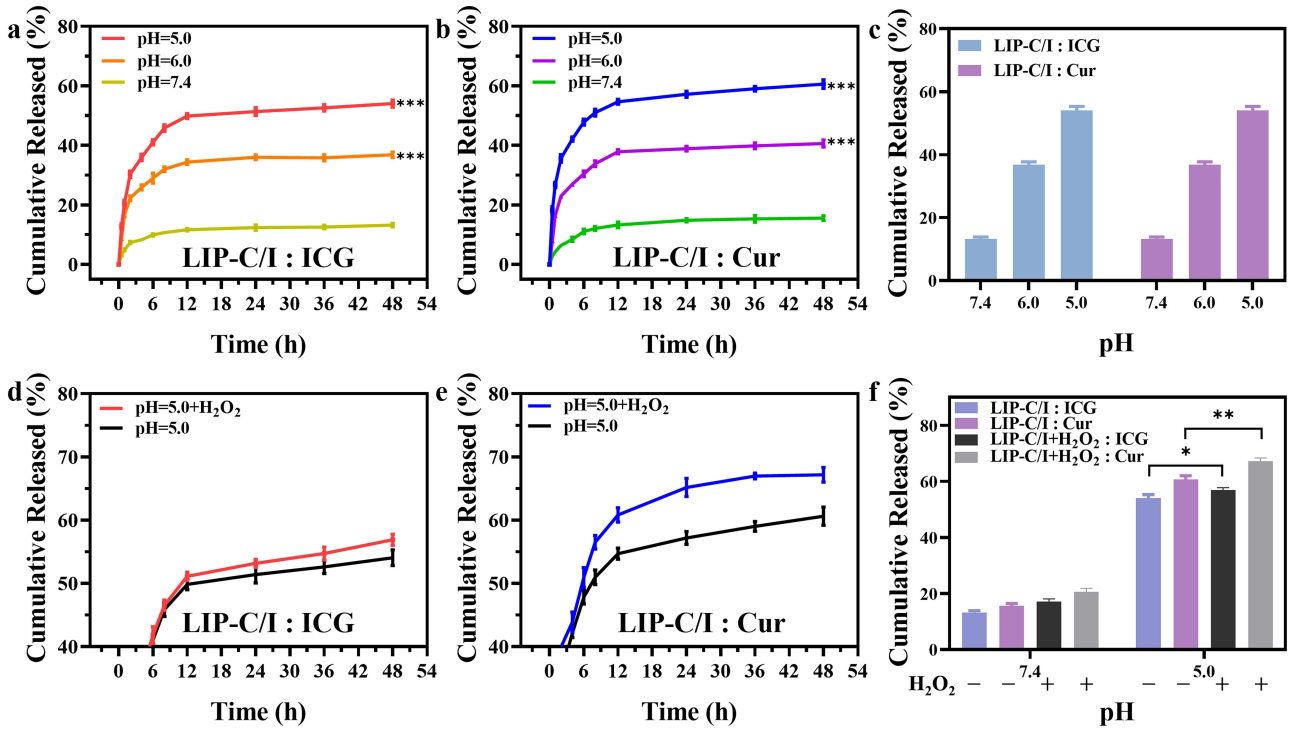

Figure 2 The kinetics of (**a**) ICG and (**b**) Cur released from LIP-C/I under various buffer conditions. ***P < 0.001 vs pH=7.4. (**c**) The chart of released comparison at different pH. The kinetics of (**d**) ICG and (**e**) Cur released with H_2O_2 treatment. (**f**) The chart of released comparison at different pH with H_2O_2 treatment and without H_2O_2 treatment. *P < 0.05, **P < 0.01.

https://doi.org/10.2147/IJN.S512590

Photothermal Conversion Efficiency

The photothermal effects of ICG and LIP-C/I were investigated by NIR laser irradiation. Initially, the photothermal conversion curves of PBS and Cur were measured, and no significant temperature increase was observed (Figure S6). To ascertain the photothermal efficacy of ICG and LIP-C/I at varying ICG concentrations (10, 20, 30, and 40 μg/mL), the solutions were subjected to 808 nm laser irradiation at an intensity of 1.5 W/cm² for a duration of 5 minutes. The consequent temperature fluctuations were meticulously documented using a thermal imaging camera. Figure 3a shows that the temperature of the LIP-C/I solution gradually increased with increasing concentration after 5 min of laser irradiation, indicating that the temperature change of LIP-C/I was positively correlated with the concentration. At 40 μg/mL, the LIP-C/I solution reached approximately 57°C, which was marginally lower than free ICG, because the ICG was encapsulated in a phospholipid bilayer of LIP-C/I. This temperature elevation also confirms that LIP-C/I possesses commendable photothermal conversion capabilities, enabling effective PTT. Figure 3b shows that the temperature of LIP-C/I significantly increased with increasing laser power. In addition, after five heating and cooling cycles, LIP-C/I maintained a stable heating effect, indicating its superior thermal stability (Figure 3c). Furthermore, the temperature rise curve of the photothermal agent ICG at different concentrations and powers was measured, and it was found that it was positively correlated with both concentration and power. At the same time, after five repeated cycles of 808 nm laser irradiation, the maximum temperature gradually dropped, indicating a gradual decline in the photothermal properties of ICG. However, after repeated 808 nm laser irradiation and cooling five times, the photothermal conversion ability of LiP-C/I remained robust, proving that ICG wrapped in LiP-C/I could improve photothermal stability (Figure 3d–f).

Biocompatibility

LIP-C/I has been proven to have excellent PTT properties and the ability to release drugs in response to the tumor environment. Considering that the biocompatibility of LIP-C/I is important for biomedical applications, L929 cell viability, hemolysis assays, and organic safety in mice were tested. The cytotoxic effects on L929 cells was assessed to evaluate whether the LIP-C/I and the drug ICG, and Cur in normal human cells had a killing effect (Figure 4a). No obvious normal cell toxicity or cell killing was found in the LIP-C/I and Cur groups at concentration of 5–25 μg/mL, the

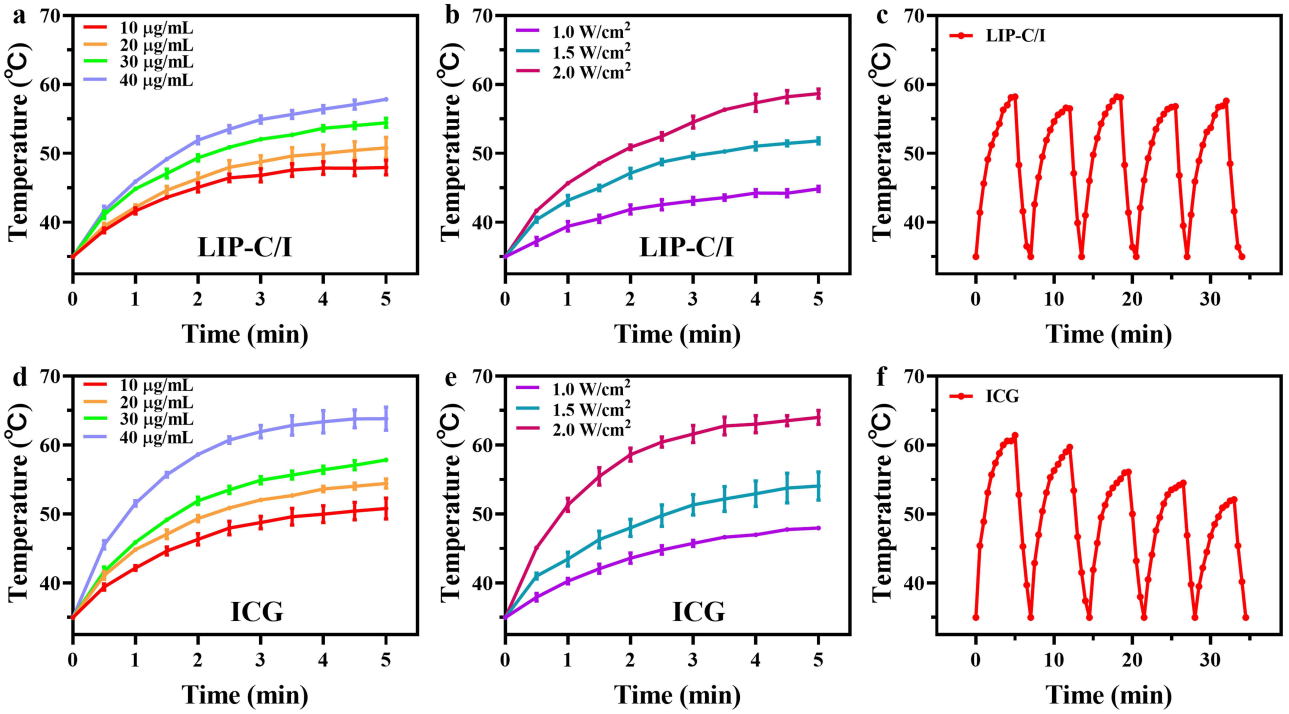

Figure 3 (**a**) temperature rise curves of LIP-C/I and (**d**) ICG under different concentrations (1.5 W/cm², 808 nm, 5 min) and (**b**) temperature rise curves of LIP-C/I and (**e**) ICG under different laser irradiation powers. Thermal stability curves of (**c**) LIP-C/I and (**f**) ICG.

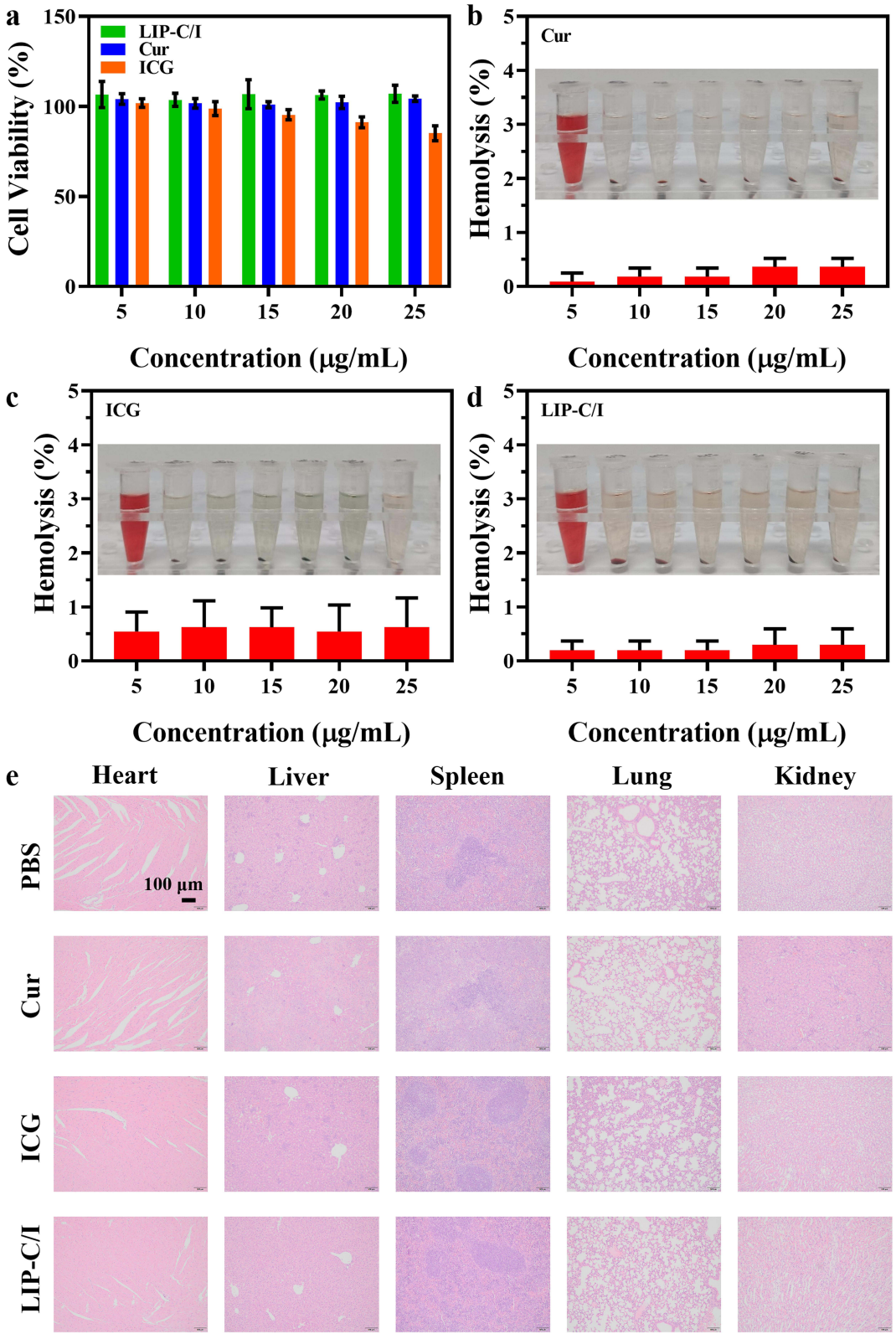

Figure 4 (**a**) Cell viability of L929 cells at the different concentrations of Cur, ICG, and LIP-C/I. Hemolysis activity of (**b**) Cur, (**c**) ICG, and (**d**) LIP-C/I. (**e**) H&E slice selection section of the major organs (heart, liver, spleen, lung, and kidney) on day 10.

https://doi.org/10.2147/IJN.S512590

ICG group had a certain killing effect on normal cells. The hemolysis rates for Cur, ICG, and LIP-C/I were each below 5%, indicating negligible hemoglobin release (Figure 4b–d). To further investigate the safety of LIP-C/I in mice, the major organs were extracted, and H&E staining was performed after injection of PBS, Cur, ICG, or LIP-C/I for 10 days. There was no damage to the organs injected with LIP-C/I compared with those injected with PBS (Figure 4e). In vitro and in vivo biosafety evaluations demonstrated that LIP-C/I is a promising material for tumor therapy.

Effect of Combination Therapy in vitro

MTT assay was used to examine the cytotoxicity of LIP-C/I in normal and tumor cells under NIR light irradiation. Figure 5a shows that the survival of L929 cells decreased with increasing ICG and LIP-C/I concentrations after laser irradiation. The ICG+NIR treatment group showed more obvious damage to normal cells than did the LIP-C/I+NIR treatment group. Owing to the good photothermal properties of LIP-C/I, LIP-C/I, which is not absorbed by cells, remains

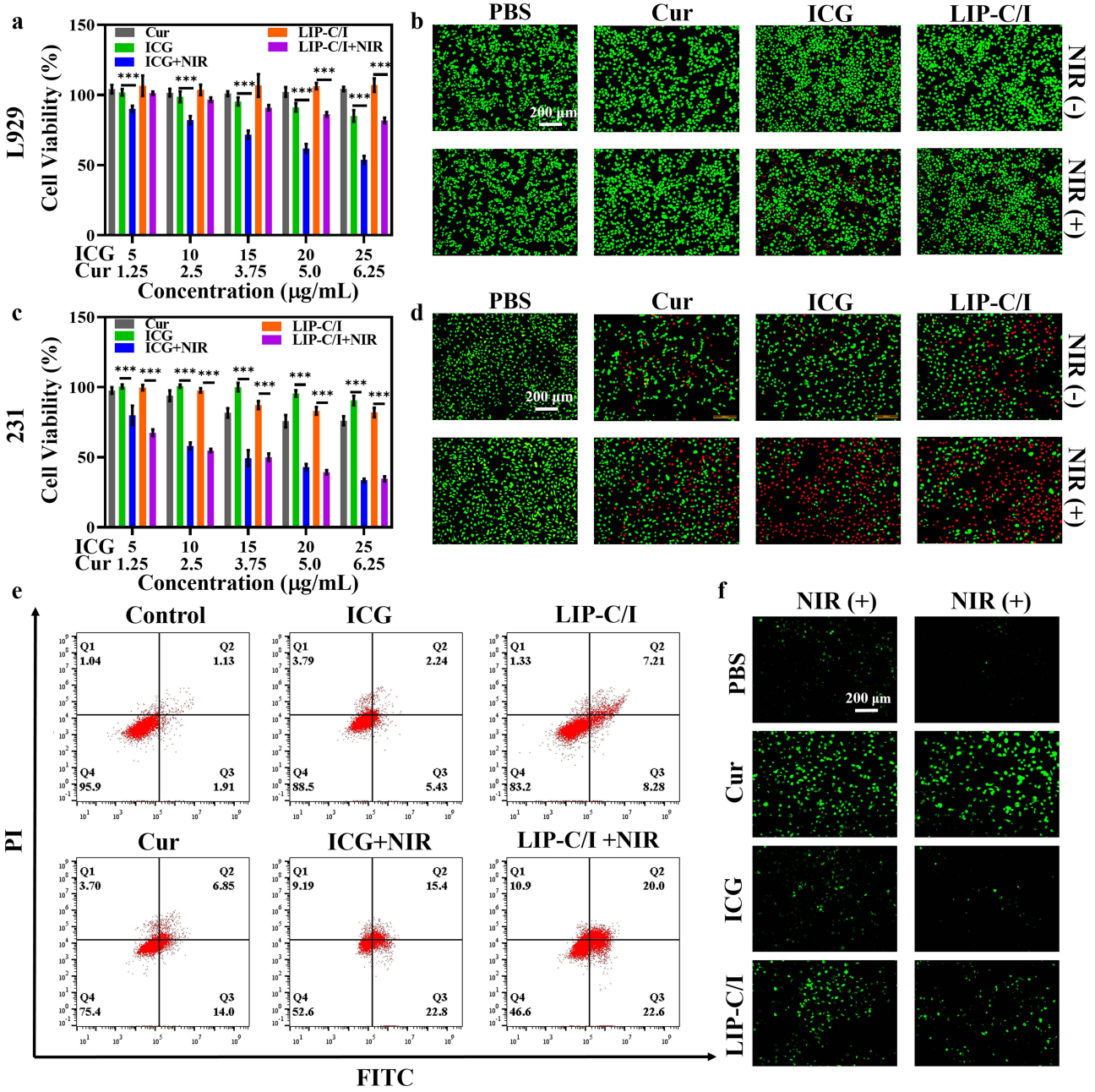

Figure 5 The MTT assay (**a–c**) and LIVE/DEAD assay (**b–d**) on both L929 and 231 cell lines, and the apoptosis rates (**e**) and ROS images (**f**) of 231 cells. ***P < 0.001.

in the medium and kills normal cells after laser irradiation. As shown in Figure 5c, the cytotoxicity of Cur, ICG, and LIP-C/I to 231 cells increased more obviously with an increase in concentration, and the killing effect was dose-dependent. All groups showed obvious cell killing after laser irradiation. To achieve a more vivid demonstration of the cytotoxic effects of nanoparticles, both the LIVE/DEAD assay and the cell apoptosis assay were employed. The observed patterns of cell death were found to be in close agreement with the outcomes of the MTT assay (Figure 5b–d). The 231 cells in the ICG and LIP-C/I groups under laser irradiation showed more red fluorescence than those in the other groups. The cell apoptosis assay results showed that the ICG+NIR and LIP-C/I+NIR groups exhibited the most pronounced cell death compared to the PBS group (Figure 5e). DCFH-DA was employed to detect intracellular ROS generation, which was visualized under an inverted fluorescence microscope (Figure 5f). In contrast to the PBS group, the Cur and LIP-C/I groups exhibited notably increased green fluorescence, indicative of elevated intracellular ROS levels attributed to the Cur's effect on ROS generation. These results showed that the ICG and LIP-C/I groups had similar killing effects on cancer cells. We speculated that the free drugs might have affected the experimental results; therefore, we replaced the medium with no drug to continue the test.

Selective Cell Killing Assay in vitro

As free drugs that are not absorbed by cells could affect cell killing, the cell medium was replaced with the no-drug medium to observe cell killing after co-culturing with drugs for six hours. Figure 6a shows that LIP-C/I caused almost no damage, indicating that LIP-C/I released less ICG in normal tissues, thus causing less damage to normal cells. The Cur, ICG, and LIP-C/I groups all showed obvious cell killing of 231 cells after laser irradiation, and the LIP-C/I+NIR group showed greater cell killing than the ICG+NIR group (Figure 6c). LIVE/DEAD experiments were performed to visualize cell death by LIP-C/I. After changing the medium, there was almost no red fluorescence in the LIP-C/I+NIR group, whereas the ICG+NIR group still showed red fluorescence, indicating that it still had a killing effect on the L929 cells (Figure 6b). The red fluorescence of 231 cells in the LIP-C/I group remained significant under laser irradiation, whereas

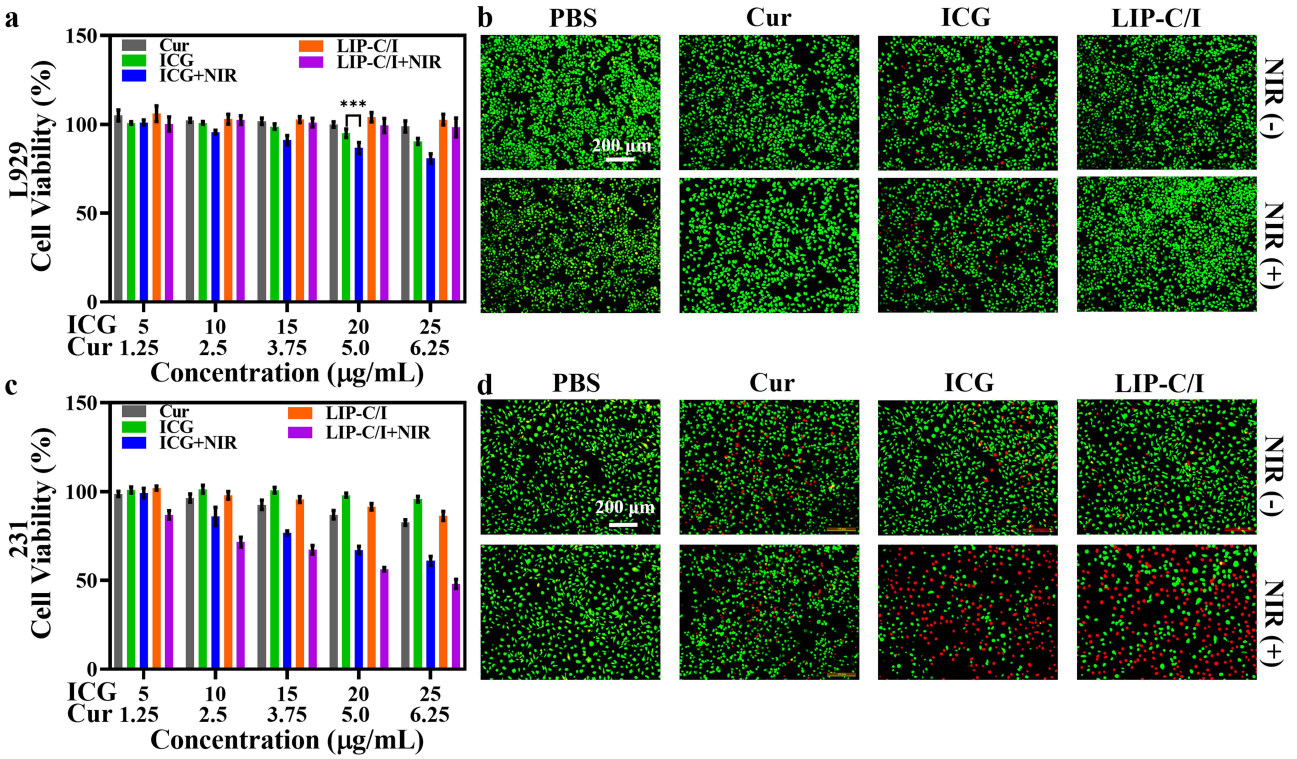

Figure 6 The MTT assay of (**a**) L929 cells and (**c**) 231 cells, and the LIVE/DEAD assay of (**b**) L929 cells and (**d**) 231 cells. The cell medium was replaced with the no-drug medium, after co-culturing with drugs for six hours. ***P < 0.001.

https://doi.org/10.2147/IJN.S512590

the red fluorescence of the other groups was reduced, and more living cells were observed (Figure 6d). These results suggest that LIP-C/I can release drugs in response to the tumor environment to selectively kill cancer cells.

Effect of Combination Therapy in vivo

To track the biological distribution of ICG in mice, an NIRF imaging system was utilized to monitor the accumulation and metabolic fate of the nanoassembly. The fluorescence intensity of ICG and LIP-C/I at the tumor sites reached a peak at 6 h and gradually decreased after 6 h, indicating that ICG and LIP-C/I could be metabolized in mice (Figure 7a). Compared with the ICG group, the LIP-C/I group showed more obvious tumor accumulation, indicating a responsive release of ICG at the tumor site. To further observe the metabolism of LIP-C/I in vivo, major organs (heart, liver, spleen, lung, and kidney) and tumors of mice were collected at 6 and 48 h (Figure 7b). The fluorescence of LIP-C/I in normal tissue was weaker than that of ICG, indicating that LIP-C/I had faster metabolism. The fluorescence of LIP-C/I in the organs was low at 48 h, indicating that metabolism was almost complete, whereas ICG still had a strong fluorescence signal in the organs, indicating that retention in the organs may cause damage to normal organs. The photothermal properties of ICG and LIP-C/I in the mice were observed 6 h after injection.

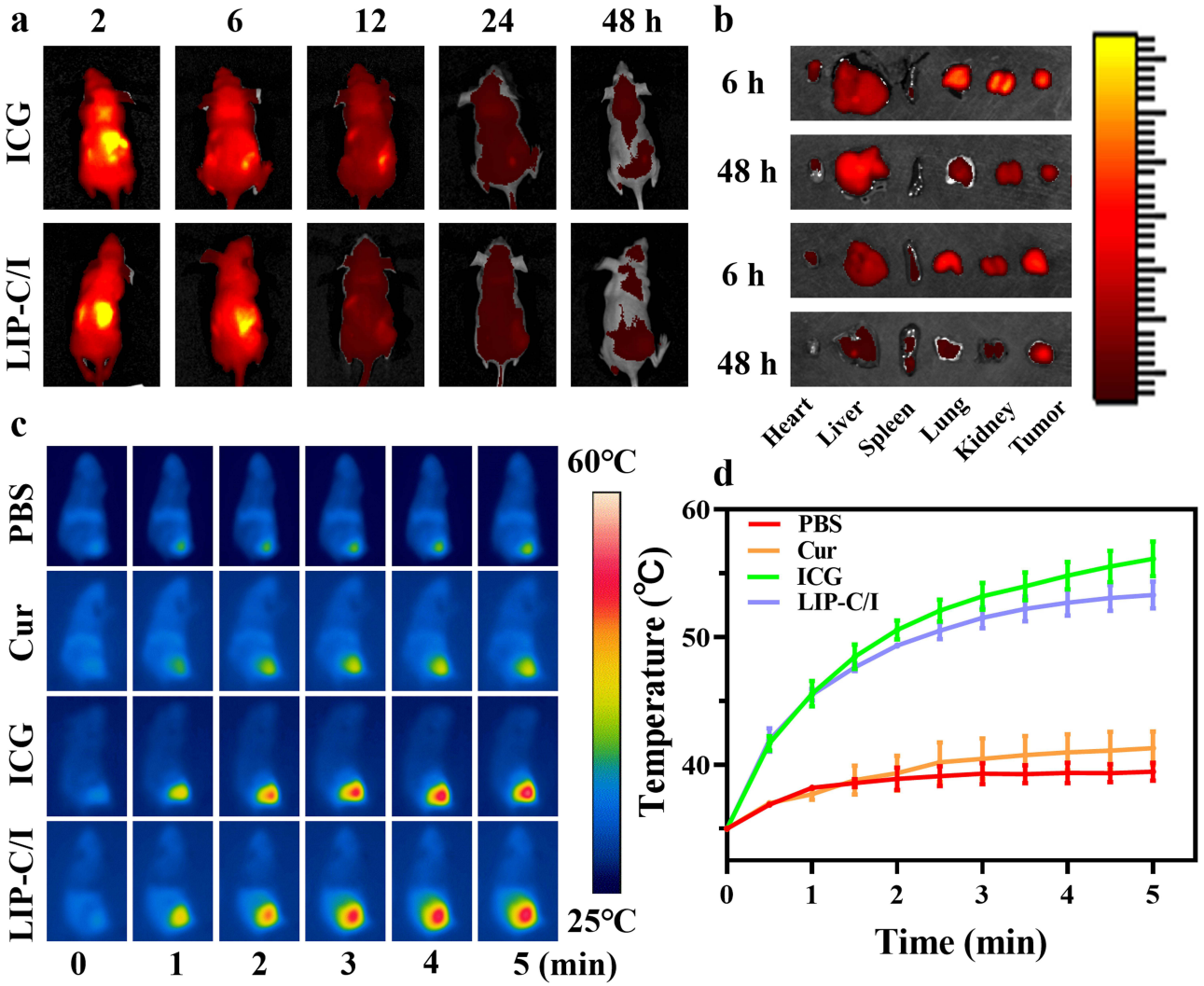

Figure 7 The fluorescence intensity in tumor-bearing nude mice was monitored over time (**a**) and the biodistribution in major organs (**b**) with samples harvested 6 hours post-administration, infrared thermal images of tumor-bearing nude mice (**c**) and the temperature progression of tumors (**d**) treated with PBS, Cur, ICG, and LIP-C/I (808 nm, 1.5 W/cm^2, 5 min).

The mice were divided into three groups (n=3): after an intraperitoneal injection for 6 h, the mice treated with PBS, Cur, ICG, and LIP-C/I were irradiated for 5 min, and the tumor surface temperatures of the mice were recorded using an infrared thermal imager. Figure 7c and d shows that the surface temperatures of the tumor sites in the PBS and Cur groups increased slightly. The ICG and LIP-C/I groups showed an obvious temperature increase, and the surface temperature of the tumor in the ICG group reached 55°C, whereas that in the LIP-C/I group reached 53°C, both of which could cause thermal damage to the tumor site.

LIP-C/I has been proven effective in killing in vitro and superior drug metabolism in vivo. Based on these experiments, the antitumor effects in mice should be further studied. Tumor-bearing mice were randomly divided into eight groups (n=4): PBS, PBS + NIR, Cur, Cur+NIR, ICG, ICG + NIR, LIP-C/I, and LIP-C/I+NIR, and intraperitoneally injected every 2 days. The weight and tumor volume of the tumor-bearing mice were measured and recorded daily, and all tumors were photographed and weighed at the end of treatment. Figure 8a illustrates that the volume expansion in the

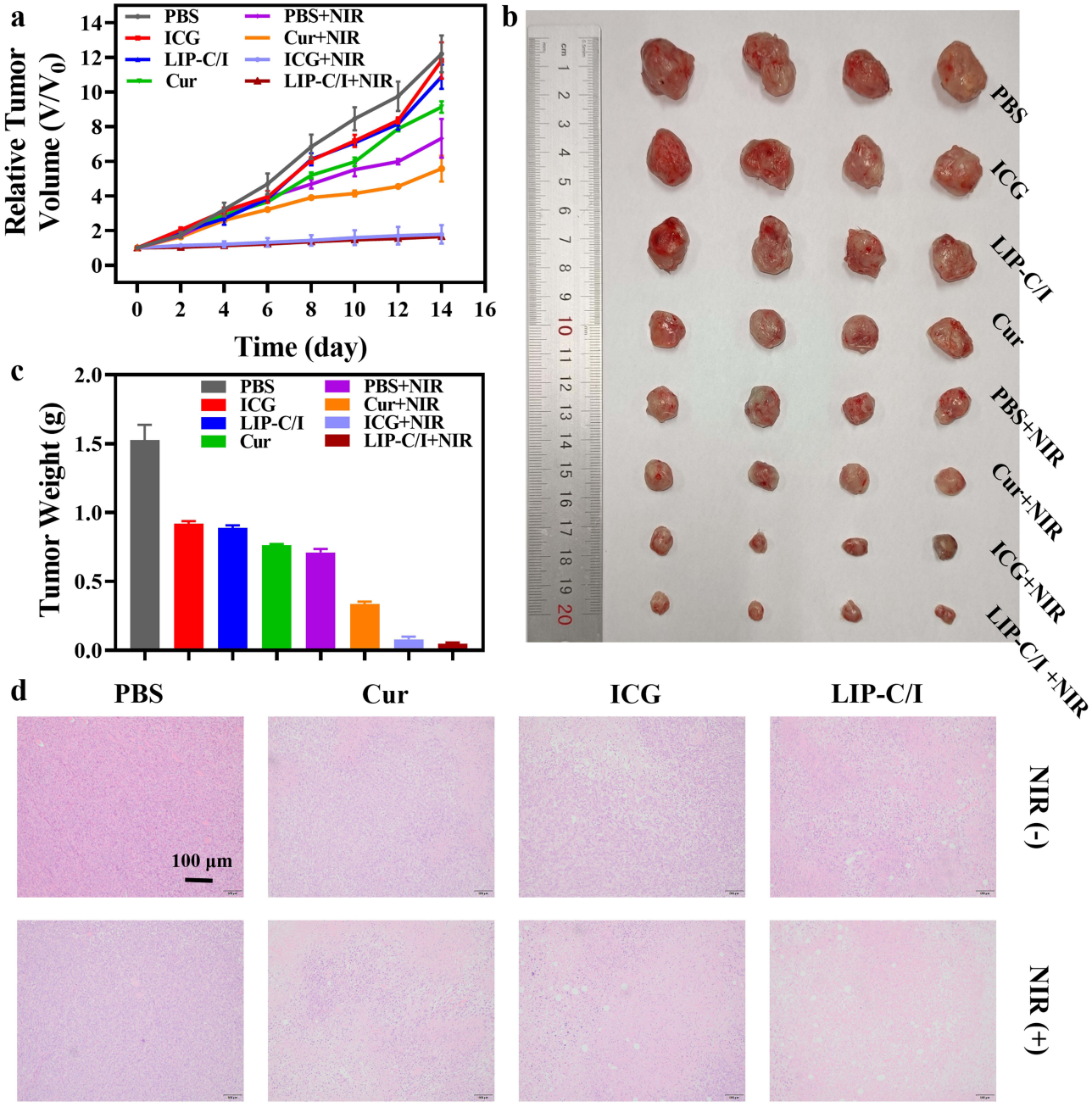

Figure 8 The tumor growth curves (**a**), tumor images (**b**), tumor weights (**c**), and H&E-stained sections (**d**) of tumors after various treatments.

https://doi.org/10.2147/IJN.S512590

ICG+NIR and LIP-C/I+NIR groups was markedly inhibited, demonstrating the most potent antitumor efficacy. Consistent with these findings, the tumor weight (Figure 8b) and digital photographs of the tumors (Figure 8c) also indicated a significant reduction. Furthermore, the effectiveness of the treatments was confirmed by histological examination with H&E staining (Figure 8d). Tumors in the ICG+NIR and LIP-C/I+NIR groups showed varying degrees of cell damage compared to the control group. These results further confirmed that our pH-responsive liposome system had an excellent combined treatment effect and showed a significant inhibitory effect on tumors.

Conclusion

In summary, we used a pH-responsive nanoassembly system to selectively treat tumor sites using dynamic covalent boronates. Dynamic self-assembly increased the solubility of Cur and pH-responsive release of Cur and ICG. The selective killing effect of LIP-C/I was proven by the results of in vitro studies, and its excellent antitumor effect was demonstrated by the results of in vivo studies. In vitro, when the cell medium was replaced with the no-drug medium, the LIP-C/I+NIR group showed the best selective cell killing effect. In vivo, The LIP-C/I+NIR group exhibited better safety under the same treatment conditions in vivo. This nanoassembly system can potentially enhance selective PTT for tumor treatment by dynamic covalent boronate, increasing the loading capacity of insoluble drugs and protecting the activity of drugs.

Data Sharing Statement

All data generated or analyzed during this study are included in this published article and in the Supporting Information.

Ethics Approval and Consent to Participate

All the rat experiments were approved by the Experimental Animal Ethics Committee of Shandong Second Medical University (2022SDL370). The husbandry and treatment of rats adhere to the requirements of the "Laboratory Animal-Guideline for Ethical Review of Animal Welfare".

Author Contributions

All authors made a significant contribution to the work reported, whether that is in the conception, study design, executive, acquisition of data, analysis, and interpretation, or in all these areas; took part in drafting, revising or critically reviewing the article; gave final approval of the version to be published; have agreed on the journal to which the article has been submitted; and agree to be accountable for all aspects of the work.

Funding

This work was supported by the National Natural Science Foundation of China (Grant Nos. 82302840 and 22301036), the Shandong Provincial Natural Science Foundation (Grant Nos. ZR2023QH038 and ZR2023MH037), Shandong Provincial Traditional Chinese Medicine Science and Technology Project (Grant Nos. Q-2023047 and M-2023084).

Disclosure

The authors declare no conflicts of interest in this work.

References

1. Jokhadze N, Das A, Dizon DS. Global cancer statistics: a healthy population relies on population health, CA. *Cancer J Clinicians*. 2024;74(3):224–226 doi:10.3322/caac.21838
2. Lopez-Perez L, Georga E, Conti C, et al. Statistical and machine learning methods for cancer research and clinical practice: a systematic review. *Biomed Signal Process Control*. 2024;92:106067. doi:10.1016/j.bspc.2024.106067
3. Singh R, Sharma A, Saji J, Umapathi A, Kumar S, Daima HK. Smart nanomaterials for cancer diagnosis and treatment. *Nano Convergence*. 2022;9 (1):21. doi:10.1186/s40580-022-00313-x
4. Qin J, Zhang J, Fan G, et al. Cold atmospheric plasma activates selective photothermal therapy of cancer. *Molecules*. 2022;27(18):5941. doi:10.3390/molecules27185941
5. Zhao L, Zhang X, Wang X, Guan X, Zhang W, Ma J. Recent advances in selective photothermal therapy of tumor. *J Nanobiotechnology*. 2021;19 (1):335. doi:10.1186/s12951-021-01080-3

6. Zhao L, Jiang M, Xu Z, et al. Selective thermotherapy of tumor by self-regulating photothermal conversion system. *J Colloid Interface Sci*. 2022;605:752–765. doi:10.1016/j.jcis.2021.07.134
7. Zhao L, Wang X, Lou H, et al. Buffet-style Cu(II) for enhance disulfiram-based cancer therapy. *J Colloid Interface Sci*. 2022;624:734–746. doi:10.1016/j.jcis.2022.06.009
8. Dou H, Luo Z, Wang H, et al. Tumor microenvironment-responsive intelligent nanoplatform with oxygen self-supply for synergistic chemotherapy/photodynamic therapy/photothermal therapy against hypoxic tumors. *Chem Eng J*. 2024;487:150523. doi:10.1016/j.cej.2024.150523
9. Yang J, Dai D, Lou X, Ma L, Wang B, Yang Y-W. Supramolecular nanomaterials based on hollow mesoporous drug carriers and macrocycle-capped CuS nanogates for synergistic chemo-photothermal therapy. *Theranostics*. 2020;10(2):615–629. doi:10.7150/thno.40066
10. Yang H, Zhang Q, Dai L, et al. Docetaxel-encapsulated catalytic Pt/Au nanotubes for synergistic chemo-photothermal therapy of triple-negative breast cancer. *Adv Healthc Mater*. 2024;13(29):e2400662. doi:10.1002/adhm.202400662
11. Jiang Z, Zhang C, Wang X, et al. A borondifluoride-complex-based photothermal agent with an 80 % photothermal conversion efficiency for photothermal therapy in the NIR-II window. *Angew Chem Int Ed Engl*. 2021;60(41):22376–22384. doi:10.1002/anie.202107836
12. Muller RH, Keck CM. Challenges and solutions for the delivery of biotech drugs–a review of drug nanocrystal technology and lipid nanoparticles. *J Biotechnol*. 2004;113(1–3):151–170. doi:10.1016/j.jbiotec.2004.06.007
13. Chao S, Lv X, Ma N, et al. A supramolecular nanoprodrug based on a boronate ester linked curcumin complexing with water-soluble pillar[5]arene for synergistic chemotherapies. *Chem Commun*. 2020;56(62):8861–8864. doi:10.1039/d0cc04315j
14. Tseng YJ, Chou SW, Shyue JJ, Lin SY, Hsiao JK, Chou PT. A versatile theranostic delivery platform integrating magnetic resonance imaging/computed tomography, pH/cis-diol controlled release, and targeted therapy. *ACS Nano*. 2016;10(6):5809–5822. doi:10.1021/acsnano.5b08130
15. Hao L, Zhou Q, Piao Y, Zhou Z, Tang J, Shen Y. Albumin-binding prodrugs via reversible iminoboronate forming nanoparticles for cancer drug delivery. *J Control Release*. 2021;330:362–371. doi:10.1016/j.jconrel.2020.12.035
16. Zhu J-Y, Lei Q, Yang B, et al. Efficient nuclear drug translocation and improved drug efficacy mediated by acidity-responsive boronate-linked dextran/cholesterol nanoassembly. *Biomaterials*. 2015;52:281–290. doi:10.1016/j.biomaterials.2015.02.048
17. Zeng X, Liu G, Tao W, et al. A drug-self-gated mesoporous antitumor nanoplatform based on pH-sensitive dynamic covalent bond. *Adv Func Mater*. 2017;27(11):1605985. doi:10.1002/adfm.201605985
18. Liang D, Shen X, Han L, et al. Dual-ROS sensitive moieties conjugate inhibits curcumin oxidative degradation for colitis precise therapy. *Adv Healthc Mater*. 2024;13(13):e2303016. doi:10.1002/adhm.202303016
19. Wang S, Chen Y, Guo J, Huang Q. Liposomes for tumor targeted therapy: a review. *Int J mol Sci*. 2023;24(3).2643. doi:10.3390/ijms24032643
20. Zhang S, Zhang Y. Promoting dual-targeting anticancer effect by regulating the dynamic intracellular self-assembly. *ACS Appl Mate Interfaces*. 2020;12(37):41105–41112 doi:10.1021/acsami.0c12271
21. Zhu Q, Saeed M, Song R, Sun T, Jiang C, Yu H. Dynamic covalent chemistry-regulated stimuli-activatable drug delivery systems for improved cancer therapy. *Chin Chem Lett*. 2020;31(5):1051–1059. doi:10.1016/j.cclet.2019.12.002
22. Zhao W, Zheng XD, Tang PY, et al. Advances of antitumor drug discovery in traditional Chinese medicine and natural active products by using multi-active components combination. *Med Res Rev*. 2023;43(5):1778–1808. doi:10.1002/med.21963
23. Yao P, Liang S, Liu Z, Xu C. A review of natural products targeting tumor immune microenvironments for the treatment of lung cancer. *Front Immunol*. 2024;15:1343316. doi:10.3389/fimmu.2024.1343316
24. Wang Y, Zeng Y, Yang W, Wang X, Jiang J. Targeting CD8(+) T cells with natural products for tumor therapy: revealing insights into the mechanisms. *Phytomedicine*. 2024;129:155608. doi:10.1016/j.phymed.2024.155608
25. Zhang J, Wu Y, Li Y, et al. Natural products and derivatives for breast cancer treatment: from drug discovery to molecular mechanism. *Phytomedicine*. 2024;129:155600. doi:10.1016/j.phymed.2024.155600
26. Zoi V, Galani V, Lianos GD, Voulgaris S, Kyritsis AP, Alexiou GA. The role of curcumin in cancer treatment. *Biomedicines*. 2021;9(9):1086. doi:10.3390/biomedicines9091086
27. Mundekkad D, Cho WC. Applications of curcumin and its nanoforms in the treatment of cancer. *Pharmaceutics*. 2023;15(9):2223. doi:10.3390/pharmaceutics15092223
28. Wang W, Li M, Wang L, Chen L, Goh BC. Curcumin in cancer therapy: exploring molecular mechanisms and overcoming clinical challenges. *Cancer Lett*. 2023;570:216332. doi:10.1016/j.canlet.2023.216332
29. Kashyap D, Tuli HS, Yerer MB, et al. Natural product-based nanoformulations for cancer therapy: opportunities and challenges. *Semin Cancer Biol*. 2021;69:5–23. doi:10.1016/j.semcancer.2019.08.014
30. Zubair H, Khan MA, Anand S, Srivastava SK, Singh S, Singh AP. Modulation of the tumor microenvironment by natural agents: implications for cancer prevention and therapy. *Semin Cancer Biol*. 2022;80:237–255 doi:10.1016/j.semcancer.2020.05.009